High-order Discontinuous Galerkin Methods for Nonhydrostatic Ocean Processes with a Free Surface

Corbin Foucart, Chris Mirabito, Patrick J. Haley, Jr., and Pierre F. J. Lermusiaux
Department of Mechanical Engineering
Massachusetts Institute of Technology
Cambridge, MA, USA
pierrel@mit.edu

***Abstract*—Accurate numerical simulation and modeling of ocean dynamics is playing an increasingly large role in scientific ocean applications. However, resolving these dynamics with traditional computational techniques can often be prohibitively expensive, necessitating the creation of next-generation high-order ocean models. In this work, we apply the local discontinuous Galerkin (LDG) and hybridizable discontinuous Galerkin (HDG) finite element methodology to discretize the ocean equations with a free-surface. We provide comparison of the strengths and weaknesses of the two formulations in terms of accuracy, efficiency, and scalability, and provide detailed discussion of numerical choices and their consequences as they relate to ocean modeling. We verify our methodology with numerical experiments and results from nonhydrostatic gravity wave theory.**

***Index Terms*—ocean modeling, ocean dynamics, finite element, high-order, nonhydrostatic, free surface**

I. Introduction

Numerical modeling of nonhydrostatic ocean dynamics is a challenging endeavor due to complicated multi-scale interactions. Ocean models typically make a hydrostatic approximation, as the horizontal length scales dominate relative to the depth scales. However, when considering ocean processes arising in regions where the depth scale is significant relative to the horizontal scale, such as in the case of flows encountering steep topography, nonhydrostatic dynamics can become important.

Discontinuous Galerkin (DG) finite element methods have been employed with a great deal of success in hydrostatic ocean models over the past few decades, especially for the shallow water equations [1]–[3]. The piecewise polynomial spaces used in DG finite element discretizations allow for high-order accuracy on unstructured grids and often provide strictly conservative numerical solutions. Moreover, DG methods are able to gracefully handle nonconforming elements and adaptive mesh refinement, an inherent limitation to classical finite element and spectral methods [1], [4]. Nonhydrostatic ocean simulations can be computationally expensive, as the nonhydrostatic pressure necessitates the solution of a globally coupled problem—however, since nonhydrostatic dynamics are typically only important in certain specific regions, an unstructured, adaptively-refined grid can allow for an efficient solution close to the cost of a hydrostatic model [5], making high-order DG methods a good candidate for nonhydrostatic ocean modeling.

Our initial research with finite element schemes was an incubation of high-order HDG schemes on 2D unstructured meshes [6]. For efficiency, legacy ocean solvers often utilize variations of projection schemes and only the pressure equation then ends up dominating costs. We thus combined the HDG method with a projection method, deriving new numerical HDG–projection-method schemes and new selective slope limiting for high-order computations. Overall, we obtained novel high-order accurate schemes for nonlinear Navier–Stokes and Boussinesq flows [7], [8]. We developed new boundary condition treatments to mitigate the formation of artificial numerical boundary layers along the bathymetry, especially in steep topographic regions. We have also explored distributed computing approaches for these methods [9]. These schemes can be employed for accurate, focused process studies of flows interacting with abrupt topography.

We have applied our HDG code to idealized non-hydrostatic dynamics. A coupled physical-biological example was used to determine that, for equivalent computational cost, high-order low-resolution simulations capture the dynamics while low-order high-resolution ones do not [6]. A lock exchange benchmark [10] showed that the non-hydrostatic solution accurately reproduces Kelvin–Helmholtz instabilities. In an idealized Stellwagen Bank test, the mode-1 Froude number and slope criticality parameter were used to determine nonlinear regimes. Coupled physical-biological simulations then revealed that non-hydrostatic physics modified primary production and significantly altered phytoplankton concentrations above the steepest slopes [7], [11]. We applied our HDG code to high-resolution simulations of internal solitary wave generation in an idealized setting [9]. These model runs capture significant overturning motions and small-scale turbulent mixing effects not observable in less computationally expensive models such as isopycnal models.

One of the novel elements of the present work is the implementation of a free surface in our high-order DG ocean model, with the option of quadrature-free and quadrature-based spatial discretization. Incorporating a free-surface in a flow simulation is problem-dependent, and common techniques for representing a free-surface include Arbitrary Lagrangian-Eulerian (ALE) methods, volume of fluid (VOF) methods, multi-layer

978-0-692-93559-0 ©2021 MTS

methods [12], [13], and level-set methods [14]. Large-scale, regional ocean modeling often involves free-surface elevations which are small compared to the depth scale, and therefore in this work we do not attempt to capture wave breaking or overturning. In the interest of computational efficiency, the model considered in this work employs a static mesh and introduces an auxiliary problem for the free-surface as a single-valued function of the horizontal coordinates of the mesh.

In this manuscript, we consider high-order DG methods developed for second-order problems, namely, the hybridizable discontinuous Galerkin (HDG) method [15], and the local discontinuous Galerkin (LDG) method [16], [17]. HDG methods involve parametrizing the local DG problem on to a trace space defined on the edges between finite elements, resulting in a reduction of globally-coupled degrees of freedom as compared to classical DG methods. The LDG method involves a weak formulation over the typical discontinuous piecewise polynomial space defined over the interior of each finite element and as such, does not enjoy the reduction of degrees of freedom as does HDG, but eliminates the need for the parametrization of the local problem onto the mesh edges, presenting a computational advantage over HDG. Both methods are mixed formulations that solve for a primal unknown as well as its gradient, but the computational trade-offs of each method in terms of accuracy, efficiency, and scalability are subtle and crucial to consider in designing a nonhydrostatic ocean model. One of the novel contributions of this work is an analysis of the impacts of the performance characteristics HDG vs. LDG methods on their respective applicability to large-scale ocean simulations.

The remainder of the paper is organized as follows. In Section II, we introduce the ocean equations and we outline our projection scheme [7] for advancing the unsteady ocean equations with a free-surface. Section III is devoted to the HDG and LDG discretizations of the projection scheme. This sets the stage for Section IV, where we discuss the scalability and performance trade-offs of the two different methods in the context of discretizations of the ocean equations. We provide numerical verification with a benchmarking set of test cases illustrating the capabilities of the model in Section V, and we conclude and provide remarks in Section VI.

II. Projection scheme

A. Governing equations

The non-hydrostatic primitive ocean equations are given as

$$\begin{aligned}\frac{\partial \boldsymbol{u}}{\partial t} - (\nabla\cdot(\nu_{xy}\nabla_{xy}\mathbf{u}) + \nabla\cdot(\nu_z\nabla_z \mathrm{w})) + \nabla p' \\ +g\nabla_{xy}\eta = -\frac{1}{\rho_0}\int_z^\eta g\nabla_{xy}\rho'\,dz' - \boldsymbol{F}_a - \boldsymbol{F}_{\text{cor}} + \frac{1}{\rho_0}\boldsymbol{f} \\ \nabla\cdot\boldsymbol{u} = 0 \\ \frac{\partial\eta}{\partial t} + \nabla\cdot\left(\int_{-H}^{\eta}\mathbf{u}\,dz\right) = 0\end{aligned} \tag{1}$$

where $\boldsymbol{F}_a = \nabla\cdot(\boldsymbol{u}\otimes\boldsymbol{u})$ is the advection term and where $\boldsymbol{F}_{\text{cor}} = f_c\hat{\boldsymbol{z}}\times\mathbf{u}$ is the Coriolis forcing with parameter f_c.

We define the total velocity $\boldsymbol{u} = [u,\, v,\, w]$, and its horizontal and vertical components $\mathbf{u} \equiv [u,\, v,\, 0]$ and $\mathrm{w} \equiv [0,\, 0,\, w]$, respectively. As convention, we take $\boldsymbol{L} \equiv \nabla\boldsymbol{u}$, such that $(\nabla\boldsymbol{u})_{ij} \equiv \frac{\partial u_i}{\partial x_j}$, and $(\nabla\cdot\boldsymbol{L})_i = \frac{\partial L_{ij}}{\partial x_j}$. We define the horizontal and vertical gradient operators $\nabla_{xy} \equiv \left[\frac{\partial}{\partial x},\, \frac{\partial}{\partial y},\, 0\right]$ and $\nabla_z \equiv \left[0,\, 0,\, \frac{\partial}{\partial z}\right]$. We denote the depth of the bathymetry as $H(x,y)$.

B. Temporal Discretization

In this section, we outline our projection scheme derived for the ocean equations in [7]. The PDEs and projections are as follows to advance the numerical solution from time k to $k+1 = k+\Delta t$.

1) Velocity predictor: We construct an intermediate velocity field $\bar{\boldsymbol{u}}^{k+1}$ which is not divergence free

$$\begin{aligned}\frac{\bar{\boldsymbol{u}}^{k+1}}{a\Delta t} - \left(\nabla\cdot\left(\nu_{xy}\nabla_{xy}\bar{\mathbf{u}}^{k+1}\right) + \nabla\cdot\left(\nu_z\nabla_z\bar{\mathrm{w}}^{k+1}\right)\right) \\ +\nabla p'^{,k} + g\nabla_{xy}\eta^k = \boldsymbol{F}_{\bar{\boldsymbol{u}}}^{k,k+1}\end{aligned}$$

subject to the boundary conditions

$$\begin{aligned}\bar{\boldsymbol{u}}^{k+1} &= \boldsymbol{g}_D \qquad \text{on } \Gamma_D, \\ \nabla\bar{\boldsymbol{u}}^{k+1}\cdot\boldsymbol{n} &= \boldsymbol{g}_N \qquad \text{on } \Gamma_N\end{aligned}$$

2) Free-surface correction: We solve a $d-1$ dimensional problem for the change in the free-surface:

$$\frac{\delta\eta^{k+1}}{a\Delta t} - \nabla\cdot\left(a\Delta t g\left(\eta^k + H\right)\nabla\delta\eta^{k+1}\right) = -\nabla\cdot\int_{-H}^{\eta^k}\bar{\mathbf{u}}^{k+1}\,dz \tag{2}$$

subject to appropriate boundary conditions.

3) Intermediate velocity projection, free-surface update:

$$\bar{\bar{\mathbf{u}}}^{k+1} = \bar{\mathbf{u}}^{k+1} - (a\Delta t)g\nabla_{xy}\delta\eta^{k+1} \tag{3}$$

$$\eta^{k+1} = \eta^k + \delta\eta^{k+1} \tag{4}$$

4) Pressure correction:

$$\nabla^2\delta p'^{,k+1} = \frac{\nabla\cdot\bar{\bar{\boldsymbol{u}}}^{k+1}}{a\Delta t} \tag{5}$$

subject to appropriate boundary conditions [7].

5) Velocity projection, pressure update:

$$\boldsymbol{u}^{k+1} = \bar{\bar{u}}^{k+1} - a\Delta t\nabla\delta p'^{,k+1}, \tag{6}$$

$$p'^{,k+1} = p'^{,k} + \delta p'^{,k+1}. \tag{7}$$

The PDE solves, namely, the velocity predictor, free-surface correction, and pressure correction steps all treat the diffusion terms implicitly to avoid an overly strict CFL limitation; the other terms are treated explicitly. As second-order parabolic and elliptic equations, an implicit discontinuous Galerkin formulation of each is recommended [4]. Since the projection steps require not only the primal unknowns, but their gradients, the mixed DG methods are a natural choice, since the gradient of the primal variable can be recovered at little extra cost, motivating the use of the LDG and HDG methods in this work.

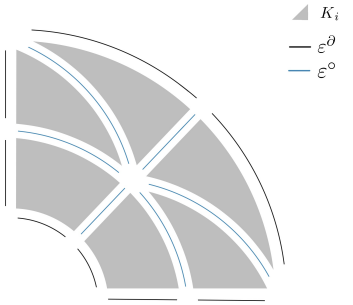

Fig. 1. Notation for domain discretization

III. Spatial Discretization

A. Notation

In order to state the weak form of the problem, we will first introduce some requisite notation. We let $\mathcal{T}_h = \cup K_i$ be a finite collection of non-overlapping elements, K_i, that discretizes the entire computational domain Ω (Figure 1). Also, let $\partial\mathcal{T}_h = \{\partial\mathcal{T}_h : K \in \mathcal{T}_h\}$ be the set of interfaces of all elements, where ∂K is the boundary of element K. For two elements sharing an edge K^+ and K^-, we define $e = \partial K^+ \cap \partial K^-$ as the edge between elements K^+ and K^-. The edges can be classified as ε° and ε^∂, the set of interior and boundary edges, respectively, with $\varepsilon = \varepsilon^\circ \cup \varepsilon^\partial$. K^+ and K^- have outward pointing normals $\boldsymbol{n}^+$ and $\boldsymbol{n}-$, respectively. The quantities $[\mathbf{a}^\pm, c^\pm]$ denote the traces of $[\mathbf{a}, c]$ on the edge e from the interior of $K^\pm$. The "mean" value $\{\{\bullet\}\}$ and "jumps" $[\![\bullet]\!]$ on the interior interfaces $e \in \varepsilon^\circ$ for scalar and vector quantities are then defined as

$$\{\{\mathbf{a}\}\} = (\mathbf{a}^+ + \mathbf{a}^-)/2, \qquad \{\{c\}\} = (c^+ + c^-)/2,$$
$$[\![\mathbf{a}]\!] = \mathbf{a}^+ \cdot \boldsymbol{n}^+ + \mathbf{a}^- \cdot \boldsymbol{n}^-, \qquad [\![c]\!] = c^+\boldsymbol{n}^+ + c^-\boldsymbol{n}^-.$$

On the set of boundary interfaces $e \in \varepsilon^\partial$, (with outward facing normal $\boldsymbol{n}$ on $\partial\Omega$), we define these mean and jump quantities the usual way:

$$\{\{\mathbf{a}\}\} = \mathbf{a}, \qquad \{\{c\}\} = c,$$
$$[\![\mathbf{a}]\!] = \mathbf{a} \cdot \boldsymbol{n}, \qquad [\![c]\!] = c\boldsymbol{n}.$$

Let $\mathcal{P}^p(D)$ denote the set of polynomials of maximum degree p existing on a domain D. We introduce the discontinuous finite element spaces:

$$W_h^p = \left\{w \in L^2(\Omega) \colon w\,|_K \in \mathcal{P}^p(K), \forall K \in \mathcal{T}_h\right\}$$
$$\boldsymbol{V}_h^p = \left\{\boldsymbol{v} \in (L^2(\Omega))^d \colon \boldsymbol{v}\,|_K \in (\mathcal{P}^p(K))^d, \forall K \in \mathcal{T}_h\right\}$$

as well as the traced finite element space

$$M_h^p = \left\{\mu \in L^2(\varepsilon_h) \colon \mu\,|_e \in \mathcal{P}^p(e), \forall e \in \varepsilon_h\right\}.$$

Lastly, we define the inner products over continuous domains $D \in \mathbb{R}^d$ and $\partial D \in \mathbb{R}^{d-1}$ as

$$(\mathbf{a}, \mathbf{b})_D = \int_D \mathbf{a} \cdot \mathbf{b}\,\mathrm{d}D \qquad (c, d)_D = \int_D cd\,\mathrm{d}D$$
$$\langle \mathbf{a}, \mathbf{b}\rangle_{\partial D} = \int_{\partial D} \mathbf{a} \cdot \mathbf{b}\,\mathrm{d}\partial D \qquad \langle c, d\rangle_{\partial D} = \int_{\partial D} cd\,\mathrm{d}\partial D$$

B. DG Formulations

To provide a unified framework for the semi-discretization of both the HDG and LDG approaches, we consider the generic second-order PDE

$$\frac{\partial u}{\partial t} - \nabla \cdot (\kappa \nabla u) = f, \tag{8}$$

We remark that the PDE in equation (8) abstractly describes both the velocity predictor and free-surface correction steps and the subsequent discretizations apply to both; the pressure correction step follows the same discretization procedure but omits the temporal derivative. Specific discretizations of the right-hand side forcing terms are given in Section III-E.

In order to arrive at either DG formulation, we consider the first order system

$$\begin{aligned} \boldsymbol{q} - \kappa\nabla u &= 0, \\ \frac{\partial u}{\partial t} - \nabla \cdot \boldsymbol{q} &= f \qquad \text{on } \Omega, \\ \boldsymbol{q} \cdot \boldsymbol{n} &= g_N \quad \text{on } \Gamma_N, \\ u &= g_D \quad \text{on } \Gamma_D, \end{aligned} \tag{9}$$

where the auxiliary variable $\boldsymbol{q}$ is a numerical representation of the gradient of the primal unknown u. Multiplying by an appropriate test function and integrating by parts over the domain yields a weak form where we seek the numerical solution $(\boldsymbol{q_h}, u_h) \in (\boldsymbol{V}_h^p, W_h^p)$ such that

$$\begin{aligned} (\boldsymbol{v}, \kappa^{-1}\boldsymbol{q}_h)_{\mathcal{T}_h} + (\nabla \cdot \boldsymbol{v}, u_h)_{\mathcal{T}_h} - \langle \boldsymbol{v} \cdot \boldsymbol{n}, \hat{u}_h\rangle_{\partial\mathcal{T}_h} &= 0, \\ \left(w, \frac{\partial u}{\partial t}\right)_{\mathcal{T}_h} + (\nabla w, \boldsymbol{q}_h)_{\mathcal{T}_h} - \langle w, \hat{\boldsymbol{q}}_h \cdot \boldsymbol{n}\rangle_{\partial\mathcal{T}_h} &= (w, f)_{\mathcal{T}_h} \end{aligned} \tag{10}$$

for all $(\boldsymbol{v}, w) \in (\boldsymbol{V}_h^p, W_h^p)$, where $\hat{\boldsymbol{q}}_h$ and $\hat{u}_h$ are the numerical fluxes approximating the quantities $\boldsymbol{q}$ and u on the element faces, respectively. The definition of the numerical fluxes $(\hat{\boldsymbol{q}}_h, \hat{u}_h)$ in terms of the approximate solution $(\boldsymbol{q}_h, u_h)$ and boundary data is sufficient to complete the description of both the LDG and HDG methods. For both methods, we perform a local elimination of the unknown $\boldsymbol{q}_h$, as the resulting linear system would otherwise be prohibitively expensive to solve.

C. LDG Formulation

We arrive at the LDG weak formulation with the choice of

$$\hat{\boldsymbol{q}}_h = \begin{cases} \{\{\boldsymbol{q}_h\}\} - \boldsymbol{\beta} \cdot [\![q_h]\!] - \tau[\![u_h]\!], & \text{on } \varepsilon_h^i \\ g_N\boldsymbol{n}, & \text{on } \varepsilon_N \\ \boldsymbol{q}_h - \tau(u_h - g_D)\boldsymbol{n}, & \text{on } \varepsilon_D \end{cases}$$

and

$$\hat{u}_h = \begin{cases} \{\{u_h\}\} + \boldsymbol{\beta} \cdot [\![u_h]\!] & \text{on } \varepsilon_h^i \\ u_h, & \text{on } \varepsilon_N \\ g_D, & \text{on } \varepsilon_D \end{cases}$$

where $\boldsymbol{\beta} = \boldsymbol{n}/2$ and τ is a stabilitization parameter on the order of the element size $\tau \sim \mathcal{O}(h^{-1})$—for additional details, see [4], [16], [18]. Making these substitutions, we can express

the generic weak form in equation (10) as the following: find $(\boldsymbol{q_h},\, u_h) \in (\boldsymbol{V}_h^p, W_h^p)$ such that

$$\begin{aligned} a(\boldsymbol{v},\, \boldsymbol{q}_h) + b(\boldsymbol{v},\, u_h) &= r(\boldsymbol{v}), \\ b^\top(w, \boldsymbol{q}_h) + c(w,\, u_h) &= f(w), \end{aligned} \tag{11}$$

for all $(\boldsymbol{v},\, w) \in (\boldsymbol{V}_h^p, W_h^p)$, where we define the bilinear forms

$$\begin{aligned} a(\boldsymbol{v}, \boldsymbol{q}_h) &= (\boldsymbol{v},\, \kappa^{-1}\boldsymbol{q}_h)_{\mathcal{T}_h} \\ b(\boldsymbol{v},\, u_h) &= (\nabla\cdot\boldsymbol{v},\, u_h)_{\mathcal{T}_h} - \langle \boldsymbol{v}\cdot\boldsymbol{n},\, u_h\rangle_{\Gamma_N} \\ &\quad - \langle \boldsymbol{v}\cdot\boldsymbol{n},\, \{\{u_h\}\} + \boldsymbol{\beta}\cdot[\![u_h]\!]\rangle_{\partial\mathcal{T}_h\setminus\Gamma} \\ b^\top(w,\, \boldsymbol{q}_h) &= (\nabla w,\, \boldsymbol{q}_h)_{\mathcal{T}_h} - \langle w,\, \boldsymbol{q}_h\cdot\boldsymbol{n}\rangle_{\Gamma_D} \\ &\quad - \langle w,\, (\{\{\boldsymbol{q}_h\}\} - [\![\boldsymbol{q}_h]\!]\boldsymbol{\beta})\cdot\boldsymbol{n}\rangle_{\partial\mathcal{T}_h\setminus\Gamma} \\ c(w,\, u_h) &= (w,\, \partial u/\partial t)_{\mathcal{T}_h} - \langle w,\, \tau u_h\rangle_{\Gamma_D} \\ &\quad - \langle w,\, \tau[\![u_h]\!]\cdot\boldsymbol{n}\rangle_{\partial\mathcal{T}_h\setminus\Gamma} \end{aligned}$$

and the linear forms

$$\begin{aligned} r(\boldsymbol{v}) &= \langle \boldsymbol{v}\cdot\boldsymbol{n},\, g_D\rangle_{\Gamma_D} \\ f(w) &= (w,\, f)_{\mathcal{T}_h} + (w,\, g_N)_{\Gamma_N} - \langle w,\, \tau g_D\rangle_{\Gamma_D}. \end{aligned}$$

Our formulation differs from the typical description in the literature in that we organize the integral operators over each element boundary ∂K, since $\partial\mathcal{T}_h = \{\partial K \colon K \in \mathcal{T}_h\}$, rather than over each interface. Due to the discontinuous nature of the DG polynomial approximation spaces and our organization of the operators over the boundary of each element, the discretization of equation (11) over each element admits the local linear system

$$\begin{pmatrix} A & B \\ B^\top & C \end{pmatrix}\begin{pmatrix} Q \\ U \end{pmatrix} = \begin{pmatrix} R \\ F \end{pmatrix}, \tag{12}$$

allowing for the elimination of the unknown $\boldsymbol{q}_h$ by way of the Schur complement with respect to the block A. The aforementioned static condensation leads to the global linear system $\mathbb{K}U = \mathbb{F}$, where

$$\begin{aligned} \mathbb{K} &= C - B^\top A^{-1} B, \\ \mathbb{F} &= F - B^\top A^{-1} R. \end{aligned} \tag{13}$$

We remark that since the linear operator A has the form of a mass matrix defined locally over each element, the inverse is cheap to compute and can even be discretized in a quadrature-free manner to avoid a dense inverse operation entirely [19].

D. HDG Formulation

For details on the HDG method, we refer to publications [15], [20]. We integrate (9) by parts over each element K and define approximations to $\boldsymbol{q}_h$ and u_h in equation (10) with the numerical traces $\widehat{\boldsymbol{q}}_h$ and $\widehat{u}_h$, respectively, defined on the element boundary ∂K as

$$\begin{aligned} \widehat{\boldsymbol{q}}_h &= \boldsymbol{q}_h - \tau\,(u_h - \widehat{u}_h)\,\boldsymbol{n}, \\ \widehat{u}_h &= \begin{cases} \mathsf{P} g_D, & \text{on } \varepsilon^\partial \cap \Gamma_D \\ \lambda_h & \text{on } \varepsilon^\circ \setminus \Gamma_D \end{cases}, \end{aligned} \tag{14}$$

where the scalar $\tau > 0$ is a stability parameter, taken as $\tau = 1$ unless otherwise specified. We additionally add a transmission condition which enforces that the normal component of the numerical flux be single-valued on each interior edge:

$$\langle \mu,\, \hat{\boldsymbol{q}}_h\cdot\boldsymbol{n}\rangle_{\partial\mathcal{T}_h\setminus\Gamma} + \langle \mu,\, \hat{\boldsymbol{q}}_h\cdot\boldsymbol{n} - g_N\rangle_{\Gamma_N} = 0. \tag{15}$$

The resulting weak form of the problem is to find $(\boldsymbol{q}_h,\, u_h,\, \lambda_h) \in (\boldsymbol{V}_h^p,\, W_h^p,\, M_h^p(0))$ such that

$$\begin{aligned} (\kappa^{-1}\boldsymbol{q}_h,\, \mathsf{v})_{\mathcal{T}_h} + (u_h,\, \nabla\cdot\mathsf{v})_{\mathcal{T}_h} - \langle \lambda_h,\, \mathsf{v}\cdot\boldsymbol{n}\rangle_{\partial\mathcal{T}_h} &= \langle \mathsf{P} g_D,\, \mathsf{v}\cdot\boldsymbol{n}\rangle_{\Gamma_D} \\ -(\nabla\cdot\boldsymbol{q}_h,\, \mathsf{w})_{\mathcal{T}_h} + \langle \tau u_h,\, \mathsf{w}\rangle_{\partial\mathcal{T}_h} - \langle \tau\lambda_h,\, \mathsf{w}\rangle_{\partial\mathcal{T}_h} &= (f,\, \mathsf{w})_{\mathcal{T}_h} \\ \langle \boldsymbol{q}_h\cdot\boldsymbol{n},\, \mu\rangle_{\partial\mathcal{T}_h\setminus\Gamma_D} - \langle \tau(u_h - \lambda_h),\, \mu\rangle_{\partial\mathcal{T}_h\setminus\Gamma_D} &= \langle \mathsf{P} g_N,\, \mu\rangle_{\Gamma_N} \end{aligned}$$

for all $(\mathsf{v}, \mathsf{w}, \mu) \in \boldsymbol{V}_h^p \times W_h^p \times M_h^p(0)$. The weak form can be expressed as [15]

$$\begin{aligned} a(\boldsymbol{q}_h,\, \mathsf{v}) + b(u_h,\, \mathsf{v}) - c(\lambda_h,\, \mathsf{v}) &= r(\mathsf{v}), \\ b(\mathsf{w},\, \boldsymbol{q}_h) - d(u_h,\, \mathsf{w}) + e(\lambda_h,\, \mathsf{w}) &= -f(\mathsf{w}), \\ c(\boldsymbol{q}_h, \mu) - g(u_h,\, \mu) + h(\lambda_h,\, \mu) &= \ell(\mu). \end{aligned} \tag{16}$$

The discretization of the integral operators in (16) results in a linear system for the unknown coefficients specifying the finite element solution $(\boldsymbol{q}_h, u_h, \lambda_h)$,

$$\begin{bmatrix} A & B & -C \\ B^T & -D & E \\ C^T & -G & H \end{bmatrix}\begin{bmatrix} Q \\ U \\ \Lambda \end{bmatrix} = \begin{bmatrix} R \\ -F \\ L \end{bmatrix}. \tag{17}$$

One of the attractive features of HDG schemes is that, due to the discontinuous nature of the approximation spaces $\boldsymbol{V}_h^p$ and W_h^p and choice of numerical flux, the matrices A B and D are block-diagonal with respect to the elements. Thus $\boldsymbol{q}_h$ and u_h can be eliminated element-by-element to yield the statically-condensed linear system for the trace variable λ_h alone, resulting in the linear system $\mathbb{K}\Lambda = \mathbb{F}$, where

$$\begin{aligned} \mathbb{K} &= H + \begin{bmatrix} C^T & -G \end{bmatrix}\begin{bmatrix} A & B \\ B^T & -D \end{bmatrix}^{-1}\begin{bmatrix} C \\ -E \end{bmatrix}, \\ \mathbb{F} &= L - \begin{bmatrix} C^T & -G \end{bmatrix}\begin{bmatrix} A & B \\ B^T & -D \end{bmatrix}^{-1}\begin{bmatrix} R \\ -F \end{bmatrix}. \end{aligned} \tag{18}$$

As we removed the degrees of freedom on Γ_D, we compute the complete approximate trace $\widehat{u}_h$ by augmenting λ_h with the boundary data g_D, and reconstruct the unknowns $\boldsymbol{q}_h$ and u_h on each element as

$$\begin{bmatrix} Q \\ U \end{bmatrix} = \begin{bmatrix} A & B \\ B^T & -D \end{bmatrix}^{-1}\left(\begin{bmatrix} 0 \\ -F_0 \end{bmatrix} + \begin{bmatrix} C \\ -E \end{bmatrix}\widehat{u}_h\right),$$

where $F_0 = (f,\, \mathsf{w})_K$ no longer includes the Dirichlet forcing data. Since $\widehat{u}_h$ is single-valued on the set of edges ε, this reconstruction can be computed on each element independently.

E. Discretization of Forcing Terms

Advection operator. To derive the discontinuous Galerkin formulation of the advection term, we integrate the advection term $(\boldsymbol{v},\, \nabla\cdot\boldsymbol{F}_a(\boldsymbol{u}_h^k))_K$ by parts to yield

$$a_h(\boldsymbol{v}, \boldsymbol{u}_h^k,\, \boldsymbol{g}_D) = -\left(\nabla\boldsymbol{v},\, \boldsymbol{F}_a(\boldsymbol{u}_h^k)\right)_K + \left\langle \boldsymbol{v},\, \boldsymbol{F}_a^*(\boldsymbol{u}_h^k, \boldsymbol{g}_D)\right\rangle_{\partial K},$$

where $\boldsymbol{F}_a^*(\boldsymbol{u}_h)$ is the numerical flux. Several choices exist, including an upwind, central, or local Lax-Friedrichs flux.

Pressure gradient operator. We apply the same procedure as above to obtain the DG formulation of the pressure gradient term $(\boldsymbol{v},\, \nabla p')_K$:

$$\mathrm{pg}_h(\boldsymbol{v}, p_h^k) = -\left(\nabla\cdot\boldsymbol{v},\, p_h'^{,k}\right)_K + \langle \boldsymbol{v},\, (p_h')^*\boldsymbol{n}\rangle_{\partial K}\,,$$

where the numerical flux is taken to be a central flux: $(p_h')^* = \{\{p_h'\}\}$. We remark that DG formulations in which the pressure gradient term is not integrated by parts, i.e., $(\boldsymbol{v},\, \nabla p_h')_K$ as in [4] have been shown to lead to instabilities in the context of high-order discontinuous Galerkin discretizations of projection methods [21].

Free-surface velocity divergence. The quantity $\bar{\boldsymbol{U}}_h \equiv \int_{-H}^{\eta^k} \bar{\boldsymbol{u}}_{xy,h}^{k+1}\, dz$ is the depth-integrated horizontal velocity, and the operator $d_h(w,,\bar{\boldsymbol{U}})$ is

$$\begin{aligned} d_h(w,\bar{\boldsymbol{U}}) &= \left(w,\, \nabla\cdot\bar{\boldsymbol{U}}\right)_K \\ &= -\left(\nabla w,\, \bar{\boldsymbol{U}}\right)_K + \left\langle w,\, \left(\bar{\boldsymbol{U}}\right)^*\cdot\boldsymbol{n}\right\rangle_{\partial K} \end{aligned}$$

where $\bar{\boldsymbol{U}}^*$ is an appropriately chosen numerical flux; here we use a central flux $\left(\bar{\boldsymbol{U}}\right)^* = \left\{\{\bar{\boldsymbol{U}}\}\right\}$.

IV. Computational Efficiency and Scaling

A. HDG vs. LDG Performance

We make the following remarks as to the strengths and weaknesses of each approach, which are not often discussed in the literature.

The introduction of the traced-finite element space M_h^p and global transmission requirement in the HDG method allows for a substantial reduction in the globally-coupled degrees of freedom as compared to the LDG and other classical DG methods, in addition to better optimal convergence properties [15]. In particular, as the polynomial order of the numerical solution increases, HDG offers increasing computational savings over the classical DG methods.

However, the computational savings due to the parametrization of the PDE onto the space M_h^p come at a cost. Comparing the elemental contributions of the two methods in equations (18) and (13), it is apparent that forming the elemental contributions and right-hand side involves an expensive matrix-inverse operation involving the local unknowns $(\boldsymbol{q}_h, u_h)$ on every element in the mesh. As the polynomial order increases, these inverses become concomitantly more expensive. This discrepancy becomes more limiting in truly large-scale simulations, where the elemental inverses can not be stored, but rather must be applied in a matrix-free manner. In this case, the memory required to store local factorizations of the elemental inverses becomes a bottleneck, moreso than the linear system itself. By comparison, the recovery of the local gradient $\boldsymbol{q}_h$ in the LDG method involves a local inverse, but only of the A operator, which is a block diagonal mass-matrix and much more cheaply invertible. Ultimately, both methods are promising for high-order ocean models, with HDG providing better accuracy and LDG providing better scalability.

B. Quadrature-free Discretization

In this work, we consider two methods for discretization of the LDG and HDG integral operators introduced in Section III. The first are quadrature-based methods using Gaussian quadrature standard in finite element methods. The second is a quadrature-free approach [22] which stores only templated mass matrices and stiffness matrices on the master element, and uses local isoparametric transformation data to form the operators in the weak form; we refer the reader to [4], [19], [22] for details. The advantage of quadrature-free discretization is the lack of a need to interpolate volume and face data to the quadrature points, instead using only nodal quantities; however, this approach comes at the cost of a reduction in accuracy and loss of symmetry, discussed in Section V.

C. Preconditioning and Iterative Solvers

Each of the PDE solves in the projection method relies on the solution of a global linear system. It is often the case that the parabolic nature of the velocity predictor and free-surface corrector equations result in linear systems which are much better conditioned compared to the pressure corrector equation. Our investigation of preconditioning strategies and efficient linear solvers for the ocean equations is still preliminary; however, we have found that both LDG and HDG schemes for ocean modeling commonly result in linear systems that are not symmetric, especially when considering quadrature-free schemes or complicated boundary condition handling. As such, we have investigated classes of iterative solvers for nonsymmetric systems—Figure 2 depicts typical convergence behavior for incomplete-LU (ILU) preconditioned pressure-corrector systems for the GMRES, BiCG-stab, and GCROT [23] iterative solvers. Preliminary results indicate that the GCROT solver routinely outperforms the others for ill-conditioned linear systems which arise in the presence of strongly nonhydrostatic dynamic regimes, and are readily improved even by mild ILU preconditioning with fill-in on the order of the sparse linear system itself.

V. Numerical Experiments

A. Spatial Verification

In order to verify our LDG and HDG finite element discretizations as formulated in Section III, we consider a steady three-dimensional convection-diffusion problem with a spatially variable, anisotropic diffusion coefficient, which mimics the implicit terms of the velocity predictor, free-surface correction, and pressure correction steps outlined in Section II.

We consider a flat-bottomed three-dimensional domain consisting of a six layer extrusion of the horizontal domain $\Omega_H = (-1,1)\times(-1,1)$, represented with a mixed mesh of both wedge and hexahedral elements (Fig. 3). The spatially variable diffusion coefficient $\kappa = (1,1,z^2)$. The source term f and Dirichlet and Neumann boundary conditions are chosen such that we have the exact solution

$$u(x,y,z) = xyz\frac{(1-e^{(x-1)})(1-e^{(y-1)})}{(1-e^{-x})(1-e^{-y})}. \qquad (19)$$

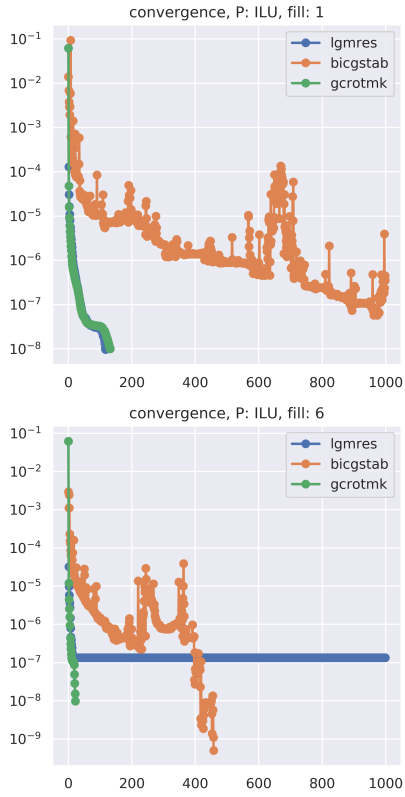

Fig. 2. Iterative solver performance for the linear solve of the 2D HDG pressure corrector equation with ILU preconditioning.

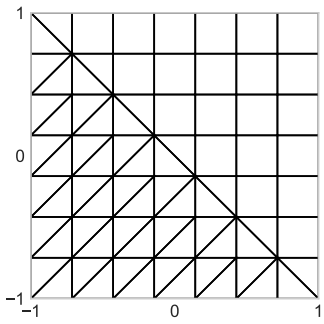

Fig. 3. Top-down view of a representative 3D wedge/hexahedral mixed mesh used in the anisotropic diffusion convergence study.

Both the LDG and HDG schemes converged optimally with respect to the scheme for 1D, 2D, and 3D versions of the test case whose exact solution is described in equation (19), at order $(p+1, p)$ for LDG discretization and $(p+1, p+1)$ for the HDG discretization for the numerical solution $(u_h, \boldsymbol{q}_h)$, respectively. Illustrative convergence results are presented for the 3D HDG test case in Figure 4 for both the quadrature-free and quadrature-based discretizations, demonstrating that there is a negligible loss in accuracy for the quadrature-free scheme.

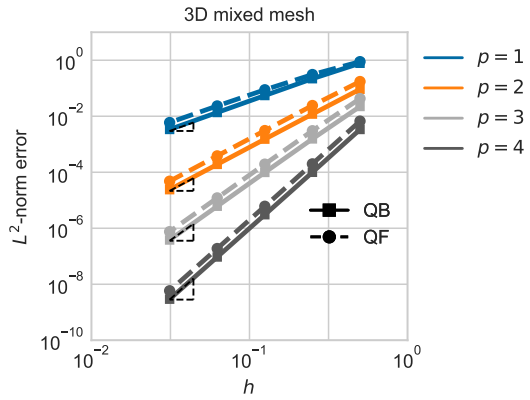

Fig. 4. History of convergence in the L^2-norm of the numerical solution u_h to the exact solution (19). Dashed lines indicate optimal convergence rates of order $p+1$ for the primal variable u_h.

B. Free-surface Seiche

To test the ability of our model to accurately represent nonhydrostatic behavior, we verify the nonhydrostatic model using linear gravity-wave theory. To do so, we simulate a free-surface seiche, similar to the test case described in [13].

For a rectangular domain of length L and depth H, the analytical solutions for the horizontal and vertical velocity of the inviscid free-surface seiche are given by

$$u = ag\frac{k}{\omega}\frac{\cosh k(z+H)}{\cosh(kH)}\sin(kx)\sin(\omega t), \tag{20}$$

$$v = -ag\frac{k}{\omega}\frac{\sinh k(z+H)}{\cosh(kH)}\cos(kx)\sin(\omega t), \tag{21}$$

with the analytical free-surface $\eta = a\cos(kx)\cos(\omega t)$. The quantity $\lambda_w = 2L$ is the fundamental wavelength and $k = 2\pi/\lambda_w$ is the wavenumber. The hydrostatic shallow-water limit is obtained as $kH \to 0$ and the nonhydrostatic deep-water limit is obtained as $kH \to \infty$.

We take as our computational domain $\Omega = [0, L] \times [-H, 0]$, with parameters

$$\begin{aligned} a &= 0.1 \text{ m} \\ L &= 7.5 \text{ m} \\ H &= 10 \text{ m} \end{aligned} \tag{22}$$

and initialize the free-surface at time $t = 0$ with the initial condition $\eta(t=0) = a\cos(kx)$. To mimic the inviscid nature of the test case, we use a small diffusion coefficient $\nu = 10^{-6}$, and the value of ω is chosen such that the seiche period is $T = 1$ s. In light of the superior convergence properties enjoyed by the method, we use the HDG formulation of the projection scheme with polynomial order $p = 3$ discontinuous elements.

We compare the analytical results for both hydrostatic and nonhydrostatic behavior given by gravity wave theory with the output of our numerical model at the end of the first seiche period. The normalized horizontal and vertical velocity profiles are plotted in Figure 6 along a depth-wise slice taken along $x = 0.2$.

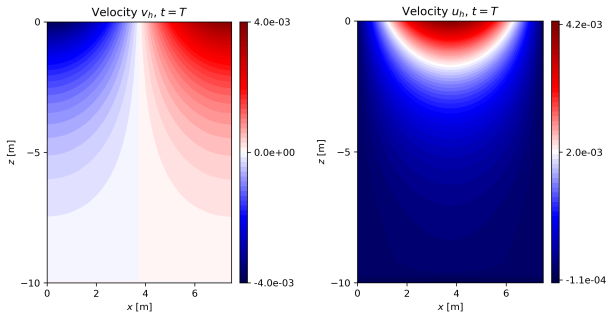

Fig. 5. Velocity fields after the completion of one seiche period.

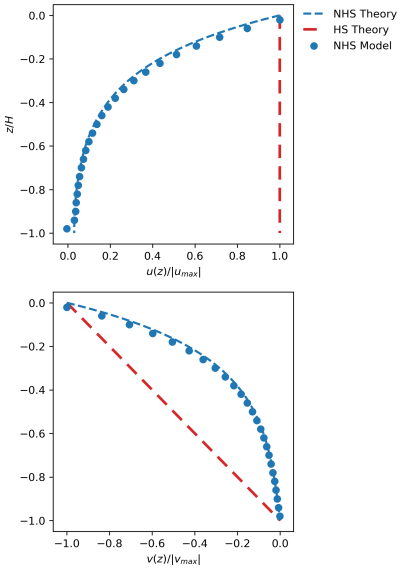

Fig. 6. Normalized horizontal (top) and vertical (bottom) velocity fields after the completion of one seiche period, compared to predictions from hydrostatic and nonhydrostatic theory.

From Figures 5 and 6, we see that the model is in good agreement with nonhydrostatic theory, in a regime which is strongly nonhydrostatic.

VI. Conclusion and Outlook

In this work, we have presented parts of a numerical model for a next-generation, high-order discontinuous Galerkin model for the ocean equations. Preliminary results show that both LDG and HDG discretizations of the model are capable of achieving high-order accuracy with both quadrature-based and quadrature-free discretizations, the latter of which can be used to improve computational efficiency in terms of memory and time-to-solution. We addressed the strengths and weaknesses of each method in terms of memory requirements, and scalability, and illustrated the ability of the high-order model to correctly capture nonhydrostatic dynamics.

We have shown that, while the HDG scheme is a more cost-effective and accurate high-order method as compared to LDG at small problem sizes, ultimately, the requirement of element-local inversion for the HDG scheme limits the scalability of this method for large-scale problems. LDG, while exhibiting lower-order convergence, removes this elemental inversion requirement, making it a candidate for truly large-scale computations. We anticipate future models which (adaptively) incorporate HDG in specific regions where high accuracy is required, and LDG in the remainder of the domain, as the underlying discontinuous nature of each method allows for a seamless combination of the two.

The investigation of model performance capturing Rayleigh–Taylor instabilities, the generation of internal waves over steep topography, and other nonhydrostatic dynamics, as well as the development of efficient matrix-free solvers for high-order mixed discontinuous Galerkin formulations in ocean modeling constitutes the subject of ongoing research.

Future work will also merge the present efforts with the Multidisciplinary Simulation, Estimation, and Assimilation Systems (MSEAS) ocean modeling for physical, acoustical, and biogeochemical studies. MSEAS [24]–[26] is used for fundamental research and for realistic simulations and forecasts of fields and uncertainties around the world's oceans [27]–[40]. Practical applications include ocean monitoring [41]; real-time acoustic predictions and DA [42]–[45]; biogeochemical-ecosystem predictions and environmental management [46]–[48]; relocatable rapid response [49], [50]; path planning for autonomous vehicles [51]–[54]; and, adaptive sampling [55]–[57]. MSEAS has been tested and validated in a wide range of real-time forecasting exercises. They include: AWACS and SW-06 [25], [33]; AOSN-II and MB-06 [27], [31], [32]; QPE-08 and -09 [44], [58], [59]; PhilEx-08 and -09 [35], [60]; NASCar and FLEAT [36], [37], [61]; and POINT [62]. The present nonhydrostatic finite-element progress may be used in such simulations and other ocean modeling software to provide new capabilities, both for research and applications.

Acknowledgments

We thank the other members of the MSEAS group for helpful discussions. We are grateful to the Office of Naval Research for support under grants N00014-15-1-2626 (DRI-FLEAT) and N00014-18-1-2781 (DRI-CALYPSO), and the National Science Foundation for support under grants EAR-1520825 (NSF-ALPHA).

REFERENCES

[1] F. X. Giraldo, J. S. Hesthaven, and T. Warburton, "Nodal high-order discontinuous Galerkin methods for the spherical shallow water equations," *Journal of Computational Physics*, vol. 181, no. 2, pp. 499–525, 2002.

[2] E. Deleersnijder and P. F. J. Lermusiaux, "Multi-scale modeling: nested-grid and unstructured-mesh approaches," *Ocean Dynamics*, vol. 58, no. 5–6, pp. 335–336, Dec. 2008.

[3] E. Deleersnijder, V. Legat, and P. F. J. Lermusiaux, "Multi-scale modelling of coastal, shelf and global ocean dynamics," *Ocean Dynamics*, vol. 60, no. 6, pp. 1357–1359, Dec. 2010.

[4] J. S. Hesthaven and T. Warburton, *Nodal Discontinuous Galerkin Methods*, ser. Texts in Applied Mathematics, J. E. Marsden, L. Sirovich, and S. S. Antman, Eds. New York, NY: Springer New York, 2008, vol. 54. [Online]. Available: http://link.springer.com/10.1007/978-0-387-72067-8

[5] O. Fringer, M. Gerritsen, and R. Street, "An unstructured-grid, finite-volume, nonhydrostatic, parallel coastal ocean simulator," *Ocean Modelling*, vol. 14, no. 3-4, pp. 139–173, Jan. 2006. [Online]. Available: https://linkinghub.elsevier.com/retrieve/pii/S1463500306000394

[6] M. P. Ueckermann and P. F. J. Lermusiaux, "High order schemes for 2D unsteady biogeochemical ocean models," *Ocean Dynamics*, vol. 60, no. 6, pp. 1415–1445, Dec. 2010.

[7] M. P. Ueckermann, "High order hybrid discontinuous Galerkin regional ocean modeling," PhD thesis, Massachusetts Institute of Technology, Department of Mechanical Engineering, Cambridge, MA, Feb. 2014.

[8] M. P. Ueckermann and P. F. J. Lermusiaux, "Hybridizable discontinuous Galerkin projection methods for Navier–Stokes and Boussinesq equations," *Journal of Computational Physics*, vol. 306, pp. 390–421, 2016.

[9] C. Foucart, C. Mirabito, P. J. Haley, Jr., and P. F. J. Lermusiaux, "Distributed implementation and verification of hybridizable discontinuous Galerkin methods for nonhydrostatic ocean processes," in *OCEANS Conference 2018*. Charleston, SC: IEEE, Oct. 2018.

[10] C. Härtel, E. Meiburg, and F. Necker, "Analysis and direct numerical simulation of the flow at a gravity-current head. Part 1. Flow topology and front speed for slip and no-slip boundaries," *Journal of Fluid Mechanics*, vol. 418, pp. 189–212, 2000.

[11] M. P. Ueckermann, C. Mirabito, P. J. Haley, Jr., and P. F. J. Lermusiaux, "High order hybridizable discontinuous Galerkin projection schemes for non-hydrostatic physical-biogeochemical ocean modeling," *Ocean Dynamics*, 2021, to be submitted.

[12] W. Pan, S. C. Kramer, and M. D. Piggott, "Multi-layer non-hydrostatic free surface modelling using the discontinuous Galerkin method," *Ocean Modelling*, vol. 134, pp. 68–83, Feb. 2019. [Online]. Available: https://linkinghub.elsevier.com/retrieve/pii/S1463500318302312

[13] S. Vitousek and O. B. Fringer, "A nonhydrostatic, isopycnal-coordinate ocean model for internal waves," *Ocean Modelling*, vol. 83, pp. 118–144, Nov. 2014. [Online]. Available: https://linkinghub.elsevier.com/retrieve/pii/S1463500314001176

[14] J. Grooss and J. S. Hesthaven, "A level set discontinuous Galerkin method for free surface flows," *Computer Methods in Applied Mechanics and Engineering*, vol. 195, no. 25-28, pp. 3406–3429, 2006.

[15] N. C. Nguyen, J. Peraire, and B. Cockburn, "An implicit high-order hybridizable discontinuous Galerkin method for linear convection–diffusion equations," *Journal of Computational Physics*, vol. 228, no. 9, pp. 3232–3254, May 2009. [Online]. Available: http://www.sciencedirect.com/science/article/pii/S0021999109000308

[16] B. Cockburn and C.-W. Shu, "The Local Discontinuous Galerkin Method for Time-Dependent Convection-Diffusion Systems," *SIAM Journal on Numerical Analysis*, vol. 35, no. 6, pp. 2440–2463, Dec. 1998. [Online]. Available: http://epubs.siam.org/doi/10.1137/S0036142997316712

[17] B. Cockburn, G. Kanschat, and D. Schötzau, "The local discontinuous Galerkin method for linearized incompressible fluid flow: a review," *Computers & Fluids*, vol. 34, no. 4-5, pp. 491–506, May 2005. [Online]. Available: https://linkinghub.elsevier.com/retrieve/pii/S0045793004000386

[18] D. N. Arnold, F. Brezzi, B. Cockburn, and L. D. Marini, "Unified Analysis of Discontinuous Galerkin Methods for Elliptic Problems," *SIAM Journal on Numerical Analysis*, vol. 39, no. 5, pp. 1749–1779, Jan. 2002. [Online]. Available: http://epubs.siam.org/doi/10.1137/S0036142901384162

[19] H. L. Atkins and C.-W. Shu, "Quadrature-free implementation of discontinuous Galerkin method for hyperbolic equations," *AIAA journal*, vol. 36, no. 5, pp. 775–782, 1998.

[20] N. C. Nguyen, J. Peraire, and B. Cockburn, "An implicit high-order hybridizable discontinuous Galerkin method for nonlinear convection–diffusion equations," *Journal of Computational Physics*, vol. 228, no. 23, pp. 8841–8855, Dec. 2009. [Online]. Available: http://www.sciencedirect.com/science/article/pii/S0021999109004756

[21] N. Fehn, W. A. Wall, and M. Kronbichler, "On the stability of projection methods for the incompressible Navier–Stokes equations based on high-order discontinuous Galerkin discretizations," *Journal of Computational Physics*, vol. 351, pp. 392–421, Dec. 2017. [Online]. Available: http://www.sciencedirect.com/science/article/pii/S0021999117306915

[22] C. Foucart, "Efficient matrix-free implementation and automated verification of hybridizable discontinuous Galerkin finite element methods," Master's thesis, Massachusetts Institute of Technology, Department of Mechanical Engineering, Cambridge, Massachusetts, Jun. 2019.

[23] J. E. Hicken and D. W. Zingg, "A simplified and flexible variant of gcrot for solving nonsymmetric linear systems," *SIAM Journal on Scientific Computing*, vol. 32, no. 3, pp. 1672–1694, 2010.

[24] MSEAS Group, "MSEAS Software," 2013. [Online]. Available: http://mseas.mit.edu/software/

[25] P. J. Haley, Jr. and P. F. J. Lermusiaux, "Multiscale two-way embedding schemes for free-surface primitive equations in the "Multidisciplinary Simulation, Estimation and Assimilation System"," *Ocean Dynamics*, vol. 60, no. 6, pp. 1497–1537, Dec. 2010.

[26] P. J. Haley, Jr., A. Agarwal, and P. F. J. Lermusiaux, "Optimizing velocities and transports for complex coastal regions and archipelagos," *Ocean Modeling*, vol. 89, pp. 1–28, 2015.

[27] P. F. J. Lermusiaux, C.-S. Chiu, G. G. Gawarkiewicz, P. Abbot, A. R. Robinson, R. N. Miller, P. J. Haley, Jr, W. G. Leslie, S. J. Majumdar, A. Pang, and F. Lekien, "Quantifying uncertainties in ocean predictions," *Oceanography*, vol. 19, no. 1, pp. 92–105, 2006.

[28] W. G. Leslie, A. R. Robinson, P. J. Haley, Jr, O. Logutov, P. A. Moreno, P. F. J. Lermusiaux, and E. Coelho, "Verification and training of real-time forecasting of multi-scale ocean dynamics for maritime rapid environmental assessment," *Journal of Marine Systems*, vol. 69, no. 1, pp. 3–16, 2008.

[29] R. Onken, A. R. Robinson, P. F. J. Lermusiaux, P. J. Haley, and L. A. Anderson, "Data-driven simulations of synoptic circulation and transports in the Tunisia-Sardinia-Sicily region," *Journal of Geophysical Research: Oceans*, vol. 108, no. C9, 2003.

[30] P. J. Haley, Jr., P. F. J. Lermusiaux, A. R. Robinson, W. G. Leslie, O. Logoutov, G. Cossarini, X. S. Liang, P. Moreno, S. R. Ramp, J. D. Doyle, J. Bellingham, F. Chavez, and S. Johnston, "Forecasting and reanalysis in the Monterey Bay/California Current region for the Autonomous Ocean Sampling Network-II experiment," *Deep Sea Research Part II: Topical Studies in Oceanography*, vol. 56, no. 3–5, pp. 127–148, Feb. 2009.

[31] A. Gangopadhyay, P. F. Lermusiaux, L. Rosenfeld, A. R. Robinson, L. Calado, H. S. Kim, W. G. Leslie, and P. J. Haley, Jr., "The California Current system: A multiscale overview and the development of a feature-oriented regional modeling system (FORMS)," *Dynamics of Atmospheres and Oceans*, vol. 52, no. 1–2, pp. 131–169, Sep. 2011, Special issue of Dynamics of Atmospheres and Oceans in honor of Prof. A. R. Robinson.

[32] S. R. Ramp, P. F. J. Lermusiaux, I. Shulman, Y. Chao, R. E. Wolf, and F. L. Bahr, "Oceanographic and atmospheric conditions on the continental shelf north of the Monterey Bay during August 2006," *Dynamics of Atmospheres and Oceans*, vol. 52, no. 1–2, pp. 192–223, Sep. 2011, Special issue of Dynamics of Atmospheres and Oceans in honor of Prof. A. R. Robinson.

[33] M. E. G. D. Colin, T. F. Duda, L. A. te Raa, T. van Zon, P. J. Haley, Jr., P. F. J. Lermusiaux, W. G. Leslie, C. Mirabito, F. P. A. Lam, A. E. Newhall, Y.-T. Lin, and J. F. Lynch, "Time-evolving acoustic propagation modeling in a complex ocean environment," in *OCEANS - Bergen, 2013 MTS/IEEE*, 2013, pp. 1–9.

[34] S. M. Kelly and P. F. J. Lermusiaux, "Internal-tide interactions with Gulf Stream and Middle Atlantic Bight shelfbreak front," *Journal of Geophysical Research: Oceans*, vol. 121, pp. 6271–6294, 2016.

[35] P. F. J. Lermusiaux, P. J. Haley, W. G. Leslie, A. Agarwal, O. Logutov, and L. J. Burton, "Multiscale physical and biological dynamics in the Philippine Archipelago: Predictions and processes," *Oceanography*, vol. 24, no. 1, pp. 70–89, 2011, Special Issue on the Philippine Straits Dynamics Experiment.

[36] P. F. J. Lermusiaux, P. J. Haley, Jr., S. Jana, A. Gupta, C. S. Kulkarni, C. Mirabito, W. H. Ali, D. N. Subramani, A. Dutt, J. Lin, A. Shcherbina, C. Lee, and A. Gangopadhyay, "Optimal planning and sampling predictions for autonomous and Lagrangian platforms and sensors in the northern Arabian Sea," *Oceanography*, vol. 30, no. 2, pp. 172–185, Jun. 2017, special issue on Autonomous and Lagrangian Platforms and Sensors (ALPS).

[37] P. F. J. Lermusiaux, D. N. Subramani, J. Lin, C. S. Kulkarni, A. Gupta, A. Dutt, T. Lolla, P. J. Haley, Jr., W. H. Ali, C. Mirabito, and S. Jana, "A future for intelligent autonomous ocean observing systems," *Journal of Marine Research*, vol. 75, no. 6, pp. 765–813, Nov. 2017, the Sea. Volume 17, The Science of Ocean Prediction, Part 2.

[38] C. S. Kulkarni, P. J. Haley, Jr., P. F. J. Lermusiaux, A. Dutt, A. Gupta, C. Mirabito, D. N. Subramani, S. Jana, W. H. Ali, T. Peacock, C. M. Royo, A. Rzeznik, and R. Supekar, "Real-time sediment plume modeling in the Southern California Bight," in *OCEANS Conference 2018*. Charleston, SC: IEEE, Oct. 2018.

[39] A. Gupta, P. J. Haley, D. N. Subramani, and P. F. J. Lermusiaux, "Fish modeling and Bayesian learning for the Lakshadweep Islands," in *OCEANS 2019 MTS/IEEE SEATTLE*. Seattle: IEEE, Oct. 2019, pp. 1–10.

[40] P. F. J. Lermusiaux, M. Doshi, C. S. Kulkarni, A. Gupta, P. J. Haley, Jr., C. Mirabito, F. Trotta, S. J. Levang, G. R. Flierl, J. Marshall, T. Peacock, and C. Noble, "Plastic pollution in the coastal oceans: Characterization and modeling," in *OCEANS 2019 MTS/IEEE SEATTLE*. Seattle: IEEE, Oct. 2019, pp. 1–10.

[41] P. F. J. Lermusiaux, P. J. Haley, Jr, and N. K. Yilmaz, "Environmental prediction, path planning and adaptive sampling: sensing and modeling for efficient ocean monitoring, management and pollution control," *Sea Technology*, vol. 48, no. 9, pp. 35–38, 2007.

[42] J. Xu, P. F. J. Lermusiaux, P. J. Haley Jr., W. G. Leslie, and O. G. Logutov, "Spatial and Temporal Variations in Acoustic propagation during the PLUSNet-07 Exercise in Dabob Bay," in *Proceedings of Meetings on Acoustics (POMA)*, vol. 4. Acoustical Society of America 155th Meeting, 2008, p. 11.

[43] F.-P. A. Lam, P. J. Haley, Jr., J. Janmaat, P. F. J. Lermusiaux, W. G. Leslie, M. W. Schouten, L. A. te Raa, and M. Rixen, "At-sea real-time coupled four-dimensional oceanographic and acoustic forecasts during Battlespace Preparation 2007," *Journal of Marine Systems*, vol. 78, no. Supplement, pp. S306–S320, Nov. 2009.

[44] P. F. J. Lermusiaux, J. Xu, C.-F. Chen, S. Jan, L. Chiu, and Y.-J. Yang, "Coupled ocean–acoustic prediction of transmission loss in a continental shelfbreak region: Predictive skill, uncertainty quantification, and dynamical sensitivities," *IEEE Journal of Oceanic Engineering*, vol. 35, no. 4, pp. 895–916, Oct. 2010.

[45] T. F. Duda, Y.-T. Lin, W. Zhang, B. D. Cornuelle, and P. F. J. Lermusiaux, "Computational studies of three-dimensional ocean sound fields in areas of complex seafloor topography and active ocean dynamics," in *Proceedings of the 10th International Conference on Theoretical and Computational Acoustics*, Taipei, Taiwan, 2011.

[46] Ş. T. Beşiktepe, P. F. J. Lermusiaux, and A. R. Robinson, "Coupled physical and biogeochemical data-driven simulations of Massachusetts Bay in late summer: Real-time and post-cruise data assimilation," *Journal of Marine Systems*, vol. 40–41, pp. 171–212, 2003.

[47] G. Cossarini, P. F. J. Lermusiaux, and C. Solidoro, "Lagoon of Venice ecosystem: Seasonal dynamics and environmental guidance with uncertainty analyses and error subspace data assimilation," *Journal of Geophysical Research: Oceans*, vol. 114, no. C6, Jun. 2009.

[48] J. Coulin, P. J. Haley, Jr., S. Jana, C. S. Kulkarni, P. F. J. Lermusiaux, and T. Peacock, "Environmental ocean and plume modeling for deep sea mining in the Bismarck Sea," in *Oceans 2017 - Anchorage*, Anchorage, AK, Sep. 2017.

[49] M. Rixen, P. F. J. Lermusiaux, and J. Osler, "Quantifying, predicting, and exploiting uncertainties in marine environments," *Ocean Dynamics*, vol. 62, no. 3, pp. 495–499, 2012.

[50] M. De Dominicis, S. Falchetti, F. Trotta, N. Pinardi, L. Giacomelli, E. Napolitano, L. Fazioli, R. Sorgente, P. J. Haley, Jr., P. F. J. Lermusiaux, F. Martins, and M. Cocco, "A relocatable ocean model in support of environmental emergencies," *Ocean Dynamics*, vol. 64, no. 5, pp. 667–688, 2014.

[51] O. Schofield, S. Glenn, J. Orcutt, M. Arrott, M. Meisinger, A. Gangopadhyay, W. Brown, R. Signell, M. Moline, Y. Chao, S. Chien, D. Thompson, A. Balasuriya, P. F. J. Lermusiaux, and M. Oliver, "Automated sensor networks to advance ocean science," *Eos Trans. AGU*, vol. 91, no. 39, pp. 345–346, Sep. 2010.

[52] T. Lolla, P. F. J. Lermusiaux, M. P. Ueckermann, and P. J. Haley, Jr., "Time-optimal path planning in dynamic flows using level set equations: Theory and schemes," *Ocean Dynamics*, vol. 64, no. 10, pp. 1373–1397, 2014.

[53] T. Lolla, P. J. Haley, Jr., and P. F. J. Lermusiaux, "Time-optimal path planning in dynamic flows using level set equations: Realistic applications," *Ocean Dynamics*, vol. 64, no. 10, pp. 1399–1417, 2014.

[54] P. F. J. Lermusiaux, T. Lolla, P. J. Haley, Jr., K. Yigit, M. P. Ueckermann, T. Sondergaard, and W. G. Leslie, "Science of autonomy: Time-optimal path planning and adaptive sampling for swarms of ocean vehicles," in *Springer Handbook of Ocean Engineering: Autonomous Ocean Vehicles, Subsystems and Control*, T. Curtin, Ed. Springer, 2016, ch. 21, pp. 481–498.

[55] P. F. J. Lermusiaux, "Adaptive modeling, adaptive data assimilation and adaptive sampling," *Physica D: Nonlinear Phenomena*, vol. 230, no. 1, pp. 172–196, 2007.

[56] K. D. Heaney, G. Gawarkiewicz, T. F. Duda, and P. F. J. Lermusiaux, "Nonlinear optimization of autonomous undersea vehicle sampling strategies for oceanographic data-assimilation," *Journal of Field Robotics*, vol. 24, no. 6, pp. 437–448, 2007.

[57] K. D. Heaney, P. F. J. Lermusiaux, T. F. Duda, and P. J. Haley, Jr., "Validation of genetic algorithm based optimal sampling for ocean data assimilation," *Ocean Dynamics*, vol. 66, pp. 1209–1229, 2016.

[58] G. Gawarkiewicz, S. Jan, P. F. J. Lermusiaux, J. L. McClean, L. Centurioni, K. Taylor, B. Cornuelle, T. F. Duda, J. Wang, Y. J. Yang, T. Sanford, R.-C. Lien, C. Lee, M.-A. Lee, W. Leslie, P. J. Haley, Jr., P. P. Niiler, G. Gopalakrishnan, P. Velez-Belchi, D.-K. Lee, and Y. Y. Kim, "Circulation and intrusions northeast of Taiwan: Chasing and predicting uncertainty in the cold dome." *Oceanography*, vol. 24, no. 4, pp. 110–121, 2011.

[59] P. F. J. Lermusiaux, P. J. Haley, Jr., G. G. Gawarkiewicz, and S. Jan, "Evaluation of multiscale ocean probabilistic forecasts: Quantifying, predicting and exploiting uncertainty," *Ocean Dynamics*, 2021, to be submitted.

[60] A. Agarwal and P. F. J. Lermusiaux, "Statistical field estimation for complex coastal regions and archipelagos," *Ocean Modelling*, vol. 40, no. 2, pp. 164–189, 2011.

[61] Y. Pan, P. J. Haley, Jr., and P. F. J. Lermusiaux, "Interactions of internal tides with a heterogeneous and rotational ocean," *Journal of Fluid Mechanics*, vol. 920, p. A18, Aug. 2021.

[62] P. F. J. Lermusiaux, C. Mirabito, P. J. Haley, Jr., W. H. Ali, A. Gupta, S. Jana, E. Dorfman, A. Laferriere, A. Kofford, G. Shepard, M. Goldsmith, K. Heaney, E. Coelho, J. Boyle, J. Murray, L. Freitag, and A. Morozov, "Real-time probabilistic coupled ocean physics-acoustics forecasting and data assimilation for underwater GPS," in *OCEANS 2020 IEEE/MTS*. IEEE, Oct. 2020, pp. 1–9.